

How does the laser beam from a laser pointer travel to the moon ?

PHY204 - Project P# 05

Victoria Amgoune, Yasmine Nourlil, Elsa Felts, and Timothey Szczepanski

Abstract This project aims to study the propagation of a laser beam from Earth to the Moon under clear atmospheric conditions. We derive the unidirectional paraxial wave equation from Maxwell's equations and implemented two numerical simulations to study which are the best-suited parameters for maximum power density achievable on the Moon's surface.

1 Introduction

This project investigates the propagation of laser beams from Earth to the Moon, with the aim of understanding how to maintain sufficient light intensity over such extreme distances. Our motivation stems from both scientific curiosity and real-world applications. Laser transmission across space has been proposed for interplanetary communication, power beaming, and experimental measurements. However, the feasibility of such systems depends critically on our ability to predict and optimize beam evolution across more than 384,000 km—through the Earth's atmosphere and the vacuum of space.

We focused on identifying the physical parameters that influence beam divergence and energy distribution at the lunar surface. In particular, we studied how the initial beam shape—Gaussian or super-Gaussian—affects the final intensity pattern, and whether beam shaping techniques can help concentrate energy at such large distances. Key questions included how much the beam spreads, how its profile deforms, and what beam parameters are optimal for delivering detectable or useful power to the lunar surface.

To model the system, we used the paraxial approximation of Maxwell's equations, which simplifies the wave equation for narrow-angle beam propagation. We assumed clear atmospheric conditions and neglected absorption and scattering in order to isolate the effects of diffraction and beam shape. Numerical simulations were performed using the Split-Step Fourier Method and the Crank–Nicolson scheme to evaluate the long-range behavior of different beam envelopes.

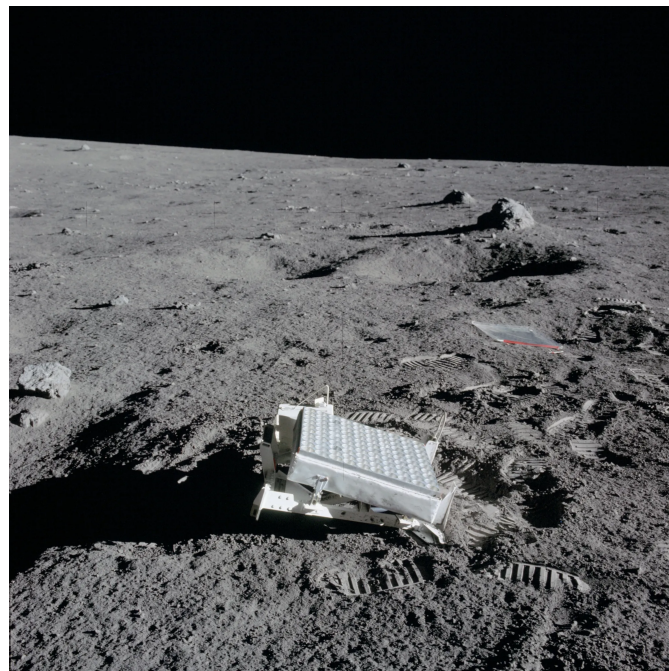
Our results show that the initial waist and envelope shape significantly affect beam spreading. Super-Gaussian beams of moderate order maintain better confinement than standard Gaussians, resulting in higher intensity at the Moon. We also observed that certain noise patterns tend to dissipate over long distances, and that power and waist tuning can greatly improve delivery efficiency. This highlights the importance of beam design in overcoming the natural divergence imposed by diffraction.

By combining theoretical modeling with numerical techniques, our work illustrates central concepts in classical electrodynamics such as diffraction, beam waist evolution, and far-field intensity distribution. It also provides a foundation for future studies incorporating more realistic effects, including atmospheric turbulence, absorption, and adaptive optics.

New questions raised by this study : what is the optimal trade-off between beam shape complexity (e.g., super-Gaussian order) and robustness to atmospheric effects? How do nonlinear effects and atmospheric turbulence alter beam confinement and intensity over large distances? What beam profiles are most resilient to real-world misalignment and optical imperfections? ...



Laser-ranging facility at the Goddard Geophysical and Astronomical Observatory in Greenbelt, Md. The facility helps NASA keep track of orbiting satellites. Both beams shown, coming from two different lasers, are pointed at NASA's Lunar Reconnaissance Orbiter, which is orbiting the Moon. Here, scientists are using the visible, green wavelength of light.



*A close-up photograph of the laser reflecting panel deployed by Apollo 14 astronauts on the Moon in 1971.
NASA*

2 Theoretical Background

To simulate the propagation of a laser beam to the Moon, we must understand how electromagnetic waves behave in space, especially over astronomical distances. In this section, we derive the mathematical

model governing beam evolution and discuss the physical parameters that influence beam spreading and intensity.

2.1 Paraxial Wave Equation

To understand how a laser beam evolves during propagation, we begin by modeling it as a monochromatic wave whose amplitude varies slowly in space and time. This is justified for well-collimated beams like Gaussian or super-Gaussian profiles. The electric field is expressed as a product of a slowly varying complex envelope $\mathcal{E}(\vec{r}, t)$ and a rapidly oscillating carrier:

$$E(\vec{r}, t) = \mathcal{E}(\vec{r}, t)e^{i(k_0 z - \omega_0 t)}$$

The envelope \mathcal{E} encodes the transverse shape and evolution of the beam, while the exponential accounts for its fast oscillations. Plugging this ansatz into the scalar wave equation, we obtain an equation governing the behavior of \mathcal{E} . (derived in Appendix B)

Physically, what emerges is that the envelope evolves mainly along the direction of propagation z , while its variation in the transverse plane (perpendicular to z) is governed by diffraction. The paraxial approximation assumes that the beam diverges only slightly and that the envelope varies slowly compared to the optical wavelength.

Under these assumptions, and neglecting temporal effects (i.e., assuming a stationary envelope), we arrive at the paraxial wave equation:

$$\nabla_{\perp}^2 \mathcal{E} + 2ik_0 \frac{\partial \mathcal{E}}{\partial z} = 0$$

This equation captures a fundamental trade-off: as the beam propagates forward, its transverse profile spreads due to diffraction. The left-hand term accounts for the transverse curvature of the beam, while the right-hand term describes its evolution along the propagation axis.

In essence, this equation provides the foundation for analyzing beam shaping, focusing, and long-distance propagation. For the detailed derivation, see Appendix B.

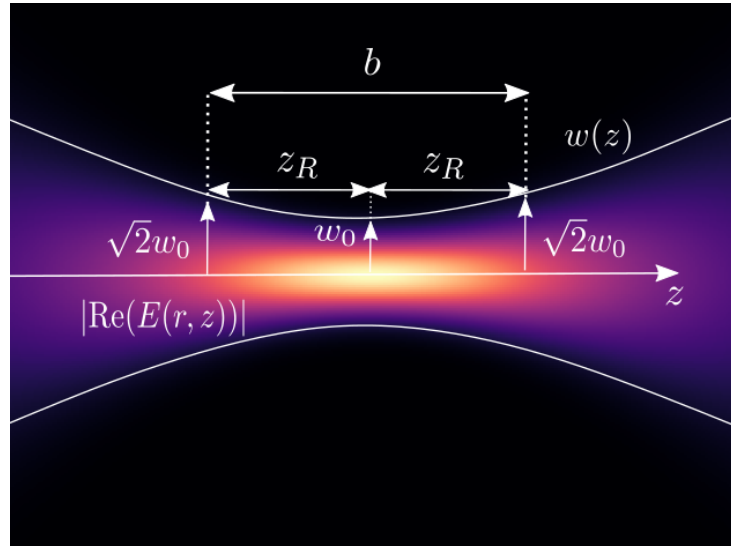
2.2 Gaussian Beam Solutions

A widely used solution to the paraxial equation is the Gaussian beam, which models the profile of many practical laser sources. For a beam with waist w_0 at $z = 0$, the solution is:

$$\mathcal{E}(r, z) = \mathcal{E}_0 \frac{w_0}{w(z)} \exp\left(-\frac{r^2}{w^2(z)}\right) \exp\left(i \frac{k_0 r^2}{2R(z)} - i\zeta(z)\right),$$

with :

$$\begin{aligned} w(z) &= w_0 \sqrt{1 + \left(\frac{z}{z_R}\right)^2}, && \text{Beam radius at } z \text{ (1/e width)} \\ R(z) &= z \left[1 + \left(\frac{z_R}{z}\right)^2\right], && \text{Wavefront curvature at } z \\ \zeta(z) &= \tan^{-1} \left(\frac{z}{z_R}\right), && \text{Gouy phase shift at } z \\ z_R &= \frac{\pi w_0^2}{\lambda}, && \text{Rayleigh range} \end{aligned}$$



Schematic representation of a Gaussian beam showing key propagation parameters: the waist w_0 , the beam width $w(z)$, and the Rayleigh range z_R . The intensity profile expands symmetrically around the focal plane, doubling its cross-sectional area over a distance $2z_R$.

This beam exhibits minimal divergence near focus, but spreads quadratically at large distances. Indeed, for $z \gg z_R$, this simplifies to: $w(z) \approx \frac{\lambda z}{\pi w_0}$. This approximation allows us to predict the spot size on the Moon. For instance, a laser pointer with waist $w_0 = 0.5$ mm and wavelength $\lambda = 532$ nm, after propagating to the Moon ($z \approx 3.8 \times 10^8$ m), gives :

$$w_{\text{moon}} \approx \frac{532 \times 10^{-9} \cdot 3.8 \times 10^8}{\pi \cdot 0.5 \times 10^{-3}} \approx 129 \text{ km.}$$

This corresponds to a beam wide enough to cover a small country. Even a well-collimated laser thus produces enormous footprints at lunar distances. This highlights why beam divergence—not power—is the main challenge when transmitting over such ranges.

2.3 Conversion of Laser Specifications to Simulation Parameters

To initialize our numerical solver and interpret its outputs in physical units, we must express the laboratory specifications of the laser—namely the waist w_0 , wavelength λ and output power P —in terms of the dimensionless parameters used in the paraxial equation. We therefore introduce the *Rayleigh range*

$$z_R = \frac{\pi w_0^2}{\lambda},$$

which sets the axial scale over which diffraction causes the beam to double its waist. For a typical green laser pointer ($w_0 = 0.5$ mm, $\lambda = 532$ nm), one finds

$$z_R \approx \frac{\pi (5 \times 10^{-4} \text{ m})^2}{5.32 \times 10^{-7} \text{ m}} \approx 1.5 \text{ m},$$

indicating that beyond a few metres of propagation the beam divergence becomes pronounced long before astronomical distances.

In our dimensionless formulation we scale the coordinates as

$$r' = \frac{r}{w_0}, \quad z' = \frac{z}{z_R},$$

so that a unit increment in z' corresponds to one Rayleigh range in physical space. Under this scaling the paraxial wave equation (3.3.1) becomes

$$\frac{\partial E'}{\partial z'} = \frac{i}{2} \nabla'^2 E',$$

where $E'(r', z') = \mathcal{E}(r, z)/E_0$ is the normalized envelope. The peak electric field E_0 is determined from the on-axis intensity

$$I_0 = \frac{2P}{\pi w_0^2} = \frac{1}{2} \varepsilon_0 c |E_0|^2 \implies E_0 = \sqrt{\frac{4P}{\pi \varepsilon_0 c w_0^2}}.$$

Expressing both coordinates and fields in these scaled units ensures that our numerical scheme remains stable and efficient even as we propagate the Moon's distance. This normalization underpins all subsequent simulations—spectral or Crank–Nicolson—by keeping the dynamic range of the variables within manageable bounds.

3 Simulation method

The numerical framework integrates two distinct approaches for solving partial differential equations: the Spectral method (Fourier-based) and the Crank–Nicolson scheme. The Spectral method is employed for its efficiency in handling periodic boundary conditions and linear terms, while the Crank–Nicolson method provides stability and accuracy for problems with Neumann boundary conditions or nonlinear source terms.

3.1 Discretization and domain

3.1.1 Principle of discretization

Both solver approaches are based on the principle of discretization of partial differential equations (PDE) which aims at replacing derivatives by finite numerical operators. They take as input a continuous equation and turn it into an algorithm computable on a discrete grid.

In our simulations, the goal is to approximate the evolution of the electric field profile $E(x, z)$ on a finite number of samples, thus we split the physical domain of computation into a finite number of points in the x and z directions. In the following, we will consider slices of $E(x, z)$ and assume it is invariant by translation along the y direction, thus reducing the number of dimensions of the problem.

Concretely, to create the grid we represent the x and z coordinates into tables using the `Numpy` library. We set the bounds of the domain as `x = np.linspace(x_min, x_max, Nx)` where `Nx` is the number of points at which we evaluate $E(x, z)$. The progress step is then defined as `dx = x[1] - x[0]` and similarly in the z direction.

The step sizes can be adapted for more or less resolution, depending on the algorithm used. At this stage, the tradeoff between accuracy and efficiency has to be taken into account to properly define `dx` and `dz`.

3.1.2 Domain and boundary handling

In theory, PDE's are not written with explicit boundaries, we impose them in the simulation to create a finite computational domain. Due to this constraint forced onto the equations, both numerical methods need to be integrated in a domain large enough so that the boundaries do not interfere with the physical solution. Indeed, the grid can act as a mirror yielding reflections and nonphysical interactions of the wave which we simulate. Two approaches can be used to avoid this situation.

In both algorithms, we implement an *adaptive window*. The idea relates to a rescaling of the box size with propagation distance. It acts on the transverse and longitudinal axis by converting the initial definition of the box in x and z variables into one based on dimensionless variables.

All variables of the equation of propagation under paraxial approximation (2.1) are first normalized and the following change of variable is made.

1. Transverse Normalization

$$\xi = \frac{x}{w_0} \Rightarrow \frac{\partial}{\partial x} = \frac{1}{w_0} \frac{\partial}{\partial \xi}$$

2. Propagation Mapping

$$\zeta(z) = \arctan\left(\frac{z}{z_R}\right) \Leftrightarrow z(\zeta) = z_R \tan \zeta$$

Working with ξ fixes the box size in the transverse direction so as to follow the enlargement of the beam and steps in ζ will translate to increasing steps in z . Therefore, we guarantee that the beam fits into the domain considering the following expression of the propagation equation,

$$\frac{\partial C}{\partial \zeta} = \frac{i}{4} \nabla_\xi^2 C + i(1 - \xi^2)C$$

where C is the transformed amplitude. The additional term $i(1 - \xi^2)$ that appears is called the potential term since it acts as a guide and acts locally on the phase of the amplitude $C(\xi, \zeta)$ to keep the beam centered at $\xi = 0$. The complete derivation of this method can be found in [1].

The only difference of implementation in the two algorithms holds in the fact that we work with the cylindrical coordinate $r = \sqrt{x^2 + y^2}$ instead of x and an additional term $\alpha(\xi)$ is added to act as an edge-absorption profile.

$$\frac{\partial C}{\partial \zeta} = \frac{i}{4} \nabla_\xi^2 C + i[1 - \xi^2]C + \alpha(\xi)C,$$

Where we discretize $\xi_j = j \Delta\xi$ and $\zeta_n = n \Delta\zeta$, form the corresponding A , B (with $\sigma = i\Delta\zeta/(4\Delta\xi^2)$), and march in ζ .

Then, we also add an *absorption mask*. The idea is to wrap the domain of computation with an artificial layer to kill the wave via an exponential decay and avoid reflections. This is done through a multiplication of the field $C(\xi, \zeta)$ by a fast decreasing exponential such as $\exp(-(\frac{\xi}{\xi_{max}})^8)$ (or a super-Gaussian).

3.2 Numerical implementation of the FFT method

In our adaptive-window approach the propagation equation acquires a nonlinear “potential” term $i[1 - \xi^2]C$ in addition to the diffraction term. We therefore employ a split-step Fourier method: at each propagation step we handle diffraction in spectral space and the potential term in real space.

We begin by discretizing the transverse coordinate ξ on a uniform grid of N_x points covering the interval $[-\xi_{\text{max}}, \xi_{\text{max}}]$. For maximal efficiency, we choose N_x (and N_z) to be powers of two, which optimizes the performance of the FFT routines (`fft2`/`ifft2`). The grid spacing is

$$\Delta\xi = \frac{2\xi_{\text{max}}}{N_x - 1}, \quad \xi_j = -\xi_{\text{max}} + j \Delta\xi, \quad j = 0, 1, \dots, N_x - 1.$$

Similarly, propagation is advanced in N_z equally spaced steps of size $\Delta\zeta$:

$$\zeta_n = n \Delta\zeta, \quad n = 0, 1, \dots, N_z - 1.$$

At each step ζ_n , the field samples are $C_j^n \approx C(\xi_j, \zeta_n)$. We compute their discrete Fourier transform \hat{C}_k^n on the wavenumber grid

$$k_{\xi_k} = \frac{2\pi}{N_x \Delta\xi} \left(k - \frac{N_x}{2} \right), \quad k = 0, 1, \dots, N_x - 1.$$

In Fourier space, the Laplacian ∇_ξ^2 becomes simple multiplication:

$$\mathcal{F}[\nabla_\xi^2 C](k_{\xi_k}) = -k_{\xi_k}^2 \hat{C}_k.$$

Accordingly, one half-step of diffraction over $\Delta\zeta/2$ is effected by

$$\hat{C}_k \mapsto \hat{C}_k \exp\left(-i \frac{k_{\xi_k}^2 \Delta\zeta}{2}\right),$$

after which an inverse FFT returns the field to real space. There we apply the potential update

$$C_j \longmapsto C_j \exp(i[1 - \xi_j^2] \Delta\zeta),$$

and finally perform the second half-step of diffraction in the same spectral manner. This sequence—FFT to spectral, multiply by diffraction phase, inverse FFT, multiply by potential phase, FFT, multiply, inverse FFT—constitutes one full propagation step $\Delta\zeta$. The split-step Fourier method thus combines spectral accuracy for diffraction with straightforward real-space handling of the nonlinear potential, enabling efficient, high-fidelity propagation to lunar distances within our expanding computational window.

$$\begin{aligned} C(\xi, \zeta + \Delta\zeta) &= \mathcal{F}^{-1} \left[e^{-\frac{i}{4} k_\xi^2 \frac{\Delta\zeta}{2}} \mathcal{F}[C(\xi, \zeta)] \right] && \text{(Half-step diffraction)} \\ &\times e^{i(1-\xi^2)\Delta\zeta} && \text{(Full potential step)} \\ &\times \mathcal{F}^{-1} \left[e^{-\frac{i}{4} k_\xi^2 \frac{\Delta\zeta}{2}} \mathcal{F}[\cdot] \right] && \text{(Half-step diffraction)} \end{aligned}$$

Algorithm 1 Beam Propagation Using the Split-Step Fourier Method

Require: Initial field envelope $C_0(\xi)$, spatial grid $\xi \in [-\xi_{\max}, \xi_{\max}]$, propagation step $\Delta\zeta$, N_z steps, wavenumbers k_ξ , potential $V(\xi) = 1 - \xi^2$

Ensure: Physical intensity $I(x, z)$ at each saved step

- 1: **Coordinate Transformations:**
- 2: $\xi = x/w_0$ (Normalized transverse coordinate)
- 3: $\zeta = \arctan(z/z_R)$ (Normalized propagation distance, $z_R = \pi w_0^2/\lambda$)
- 4: \Rightarrow Physical distance recovered as $z = z_R \tan \zeta$
- 5: Compute half-step diffraction operator: $H_{\text{half}} \leftarrow \exp \left(i \frac{k_\xi^2}{4} \cdot \frac{\Delta\zeta}{2} \right)$
- 6: Compute full-step potential operator: $P \leftarrow \exp(iV(\xi) \cdot \Delta\zeta)$
- 7: Define attenuation mask: $M(\xi) \leftarrow \exp(-(\xi/\xi_{\max})^8)$
- 8: Initialize field: $C \leftarrow C_0$
- 9: **for** $n = 0$ to $N_z - 1$ **do**
- 10: **if** $n \bmod (N_z/300) = 0$ **or** $n = N_z - 1$ **then**
- 11: Store field C and corresponding z_n
- 12: **end if**
- 13: $\hat{C} \leftarrow \mathcal{F}[C]$ {FFT to spectral space}
- 14: $\hat{C} \leftarrow H_{\text{half}} \cdot \hat{C}$
- 15: $C \leftarrow \mathcal{F}^{-1}[\hat{C}]$ {Back to real space}
- 16: $C \leftarrow P \cdot C$ {Full-step potential}
- 17: $\hat{C} \leftarrow \mathcal{F}[C]$
- 18: $\hat{C} \leftarrow H_{\text{half}} \cdot \hat{C}$
- 19: $C \leftarrow \mathcal{F}^{-1}[\hat{C}]$
- 20: $C \leftarrow M \cdot C$ {Apply attenuation mask}
- 21: **end for**
- 22: Normalize intensity: $I(\xi, z) \leftarrow |C(\xi, z)|^2 / \max(|C|^2)$
- 23: Convert to physical space: $x = \xi w_0$, $z = n \Delta z$
- 24: **for** each propagation step z_n **do**
- 25: Compute beam width $w(z_n) = w_0 \sqrt{1 + (z_n/z_R)^2}$
- 26: Transform $\xi \rightarrow x$ using $x = \xi w(z_n)$
- 27: Normalize intensity: $I(x, z_n) = |C(\xi, z_n)|^2 / w(z_n)^2$
- 28: **end for**
- 29: Interpolate intensity on a regular x -grid for visualization =0

3.2.1 Spectral Accuracy and Absence of Truncation Error

A major strength of FFT-based methods is the absence of truncation error when computing spatial derivatives. In contrast to finite difference schemes, where derivatives are approximated locally and incur errors depending on the grid spacing, Fourier methods compute the derivative exactly in the spectral domain:

$$\mathcal{F} [\nabla_\perp^2 A(x, y, z)] = -(k_x^2 + k_y^2) \hat{A}(k_x, k_y, z).$$

This operation applies the Laplacian exactly to the trigonometric interpolant of the sampled data, avoiding any truncation of Taylor expansions.

3.2.2 Complexity of the FFT-based methods

A key strength of the Fast Fourier Transform (FFT) is its low computational complexity. While a naive Discrete Fourier Transform (DFT) requires $\mathcal{O}(N^2)$ operations, the FFT reduces this to $\mathcal{O}(N \log N)$. This efficiency is crucial when simulating laser beam propagation over large spatial domains and long distances, such as from Earth to the Moon. (to see the explanation, view Appendix C)

3.2.3 Memory and Runtime Benefits

The runtime of an algorithm refers to the amount of time it takes to complete a computation as a function of the input size. In our case, the total runtime will then scale with the number of steps in z :

$$\text{total runtime} = \#\text{steps} \times \mathcal{O}(N \log N)$$

For Fourier-based methods, the Fast Fourier Transform (FFT) significantly reduces runtime compared to naive approaches by lowering the computational complexity per step.

Since the FFT does not require storing large matrices (as in matrix-vector products for DFTs), it is also more memory-efficient. Most FFT implementations are in-place and require only minimal temporary storage, meaning they overwrite the input array with the output to minimize memory usage. This is especially advantageous when simulating systems with large spatial grids and many time or distance steps, where memory and storage become limiting factors.

In summary, the $\mathcal{O}(N \log N)$ scaling of the FFT is essential for making large-scale simulations computationally feasible. It allows us to simulate long-distance beam propagation with high accuracy, low memory overhead, and fast execution time—making it an ideal choice for modeling laser transmission across astronomical scales.

3.3 The Crank-Nicolson Method

The Crank-Nicolson method is a finite-difference numerical scheme that discretizes both spatial and longitudinal derivatives using centered differences. It is particularly advantageous for the paraxial wave equation due to its second-order accuracy in both spatial and propagation dimensions and its unconditional stability for linear equations, making it ideal for simulations over large propagation distances.

3.3.1 Discretization of the Paraxial Wave Equation

Starting from the cylindrical-coordinate paraxial wave equation with radial symmetry:

$$\frac{\partial \mathcal{E}(r, z)}{\partial z} = \frac{i}{2k_0} \left(\frac{\partial^2 \mathcal{E}}{\partial r^2} + \frac{1}{r} \frac{\partial \mathcal{E}}{\partial r} \right),$$

we discretize the spatial domain into radial points $r_j = j\Delta r$, $j = 0, \dots, J - 1$, and longitudinal points $z_n = n\Delta z$, $n = 0, \dots, N - 1$. Let us denote the discretized field as $\mathcal{E}_j^n \approx \mathcal{E}(r_j, z_n)$. Using the Crank-Nicolson scheme, we approximate the longitudinal derivative using the midpoint rule :

$$\frac{\mathcal{E}_j^{n+1} - \mathcal{E}_j^n}{\Delta z} = \frac{i}{4k_0} \left[\left(\frac{\partial^2}{\partial r^2} + \frac{1}{r} \frac{\partial}{\partial r} \right) \mathcal{E}_j^{n+1} + \left(\frac{\partial^2}{\partial r^2} + \frac{1}{r} \frac{\partial}{\partial r} \right) \mathcal{E}_j^n \right].$$

3.3.2 Finite-Difference Scheme and Linear System

To approximate spatial derivatives, we apply centered differences:

$$\frac{\partial^2 \mathcal{E}}{\partial r^2} \Big|_{r_j} \approx \frac{\mathcal{E}_{j+1} - 2\mathcal{E}_j + \mathcal{E}_{j-1}}{\Delta r^2}, \quad \frac{1}{r} \frac{\partial \mathcal{E}}{\partial r} \Big|_{r_j} \approx \frac{\mathcal{E}_{j+1} - \mathcal{E}_{j-1}}{2r_j \Delta r}.$$

Defining the parameter:

$$\sigma = \frac{i\Delta z}{4k_0 \Delta r^2},$$

the discretized equation at interior points $1 \leq j \leq J - 2$ becomes:

$$\begin{aligned} -\sigma \left(1 - \frac{1}{2j}\right) \mathcal{E}_{j-1}^{n+1} + (1 + 2\sigma) \mathcal{E}_j^{n+1} - \sigma \left(1 + \frac{1}{2j}\right) \mathcal{E}_{j+1}^{n+1} \\ = \sigma \left(1 - \frac{1}{2j}\right) \mathcal{E}_{j-1}^n + (1 - 2\sigma) \mathcal{E}_j^n + \sigma \left(1 + \frac{1}{2j}\right) \mathcal{E}_{j+1}^n. \end{aligned}$$

This scheme can be expressed compactly in matrix form as:

$$A\mathbf{U}^{n+1} = B\mathbf{U}^n,$$

where \mathbf{U}^n contains discretized field values at step n , and matrices A and B are tridiagonal with elements derived from Equation (??).

3.3.3 Implementation of Neumann Boundary Conditions

To enforce the Neumann boundary conditions at the radial edges ($\partial_r \mathcal{E} = 0$), we use ghost nodes at both ends of the spatial domain:

$$\mathcal{E}_{-1}^n = \mathcal{E}_1^n, \quad \mathcal{E}_J^n = \mathcal{E}_{J-2}^n.$$

These yield modified update rules at the boundaries which preserve symmetry and prevent spurious reflections:

- At $j = 0$, the forward and backward update is given by:

$$(1 + 4\sigma) \mathcal{E}_0^{n+1} - 4\sigma \mathcal{E}_1^{n+1} = (1 - 4\sigma) \mathcal{E}_0^n + 4\sigma \mathcal{E}_1^n.$$

- At $j = J - 1$:

$$-4\sigma \mathcal{E}_{J-2}^{n+1} + (1 + 4\sigma) \mathcal{E}_{J-1}^{n+1} = 4\sigma \mathcal{E}_{J-2}^n + (1 - 4\sigma) \mathcal{E}_{J-1}^n.$$

These conditions are incorporated directly into the first and last rows of the Crank–Nicolson matrices A and B , altering their otherwise tridiagonal structure to properly reflect the zero-derivative (reflective) boundary conditions.

The matrix A governs the forward evolution step \mathbf{U}^{n+1} and includes **diagonal entries** representing self-coupling, **boundary-specific terms** that enforce the Neumann condition at $j = 0$ and $j = J - 1$, and off-diagonal elements controlling the internal second-order diffusion.

$$A = \begin{bmatrix} 1 + 4\sigma & -4\sigma & 0 & \cdots & 0 & 0 \\ -\sigma \left(1 - \frac{1}{2}\right) & 1 + 2\sigma & -\sigma \left(1 + \frac{1}{2}\right) & \cdots & 0 & 0 \\ 0 & -\sigma \left(1 - \frac{1}{3}\right) & 1 + 2\sigma & \cdots & 0 & 0 \\ \vdots & \vdots & \ddots & \ddots & \vdots & \vdots \\ 0 & 0 & \cdots & -\sigma \left(1 - \frac{1}{2j}\right) & 1 + 2\sigma & -\sigma \left(1 + \frac{1}{2j}\right) \\ 0 & 0 & \cdots & 0 & -4\sigma & 1 + 4\sigma \end{bmatrix}$$

The matrix B appears on the right-hand side of the system and encodes the known data from the previous propagation step. It contains **diagonal entries** that mirror those in A , but with opposite sign on σ , **boundary coefficients** for the Neumann update at $j = 0$ and $j = J - 1$ and off-diagonal couplings contributing to the time-centering of the Crank–Nicolson scheme.

$$B = \begin{bmatrix} 1 - 4\sigma & 4\sigma & 0 & \cdots & 0 & 0 \\ \sigma \left(1 - \frac{1}{2}\right) & 1 - 2\sigma & \sigma \left(1 + \frac{1}{2}\right) & \cdots & 0 & 0 \\ 0 & \sigma \left(1 - \frac{1}{3}\right) & 1 - 2\sigma & \cdots & 0 & 0 \\ \vdots & \vdots & \ddots & \ddots & \vdots & \vdots \\ 0 & 0 & \cdots & \sigma \left(1 - \frac{1}{2j}\right) & 1 - 2\sigma & \sigma \left(1 + \frac{1}{2j}\right) \\ 0 & 0 & \cdots & 0 & 4\sigma & 1 - 4\sigma \end{bmatrix}$$

Because these matrices remain constant in time, they are factored once and reused efficiently throughout the propagation. And the resulting linear system at each propagation step is tridiagonal, enabling efficient numerical solution via specialized solvers (for instance the Thomas algorithm). This significantly reduces computational effort, ensuring numerical stability and accuracy even over large propagation distances.

3.3.4 Algorithmic Outline

Algorithm 2 Beam Propagation Using Crank–Nicolson in Physical (r, z) Space

Require: Initial envelope $\mathcal{E}_0(r_j)$ on grid $r_j = j \Delta r$, $j = 0, \dots, J - 1$, propagation step Δz , total steps N_z , wavenumber k_0

Ensure: Envelope $\mathcal{E}(r, z)$ at each saved z_n

1: **Precompute:**

$$2: \quad D \leftarrow \frac{i}{2k_0}$$

$$3: \quad \sigma \leftarrow \frac{D \Delta z}{2 \Delta r^2} = \frac{i \Delta z}{4 k_0 \Delta r^2}$$

4: Assemble tridiagonal matrices A and B from Eq. (??),
5: with first/last rows enforcing Neumann BC:

$$\mathcal{E}_{-1} = \mathcal{E}_1, \quad \mathcal{E}_J = \mathcal{E}_{J-2}$$

6: Pre-factorize A (Thomas algorithm)

$$7: \quad \mathbf{E} \leftarrow (\mathcal{E}_0(r_0), \dots, \mathcal{E}_0(r_{J-1}))^\top$$

8: **for** $n = 0$ **to** $N_z - 1$ **do**

9: **b** $\leftarrow B \mathbf{E}$

10: Solve $A \mathbf{E} = \mathbf{b}$ {Tridiagonal solve for \mathbf{E}^{n+1} }

11: **if** $n \bmod (N_z/100) = 0$ **or** $n = N_z - 1$ **then**

12: Save \mathbf{E} and $z_n = n \Delta z$

13: **end if**

14: **end for**

15: **Post-process:**

16: Compute physical intensity:

$$I(r_j, z_n) = |\mathcal{E}_j^n|^2$$

17: (Optional) Normalize, extract beam-width, etc. =0

Algorithm 3 Beam Propagation Using Crank–Nicolson in Computational Space

Require: Initial envelope $C_0(\xi)$ on grid $\xi_j \in [-\xi_{\max}, \xi_{\max}]$, steps $\Delta\zeta$, total steps N_ζ , absorption profile $\alpha(\xi)$
Ensure: Envelope $C(\xi, \zeta)$ at saved propagation distances

```

1: Precompute:
2:    $\sigma \leftarrow \frac{i \Delta\zeta}{4 \Delta\xi^2}$ 
3:   Assemble tridiagonal matrices  $A$  and  $B$  from Eq. (??),
4:     with first/last rows for Neumann BC
5:   Pre-factorize  $A$  (Thomas algorithm)
6:    $C \leftarrow C_0$  {Initial field in comp. space}
7: for  $n = 0$  to  $N_\zeta - 1$  do
8:    $\mathbf{b} \leftarrow B \mathbf{C}$ 
9:   Solve  $A \mathbf{C} = \mathbf{b}$  {Tridiagonal solve}
10:   $\mathbf{C} \leftarrow \exp(-\alpha(\xi) \Delta\zeta) \mathbf{C}$  {Absorb edges}
11:  if  $n \bmod (N_\zeta/100) = 0$  or  $n = N_\zeta - 1$  then
12:    Save  $C(\xi, \zeta_n)$  and  $z_n = z_R \tan \zeta_n$ 
13:  end if
14: end for
15: Postprocess (optional):
16:   Recover physical field:

```

$$E(r, z) = \frac{w(z)}{w_0} \exp[-i \phi(r, z)] C(\xi, \zeta)$$

```
17: Compute intensity  $I(r, z) = |E(r, z)|^2 = 0$ 
```

The tridiagonal structure of A and B allows an $\mathcal{O}(J)$ Thomas-algorithm solver at each step. The edge-absorption $\exp(-\alpha \Delta\zeta)$ suppresses spurious reflections without any extra boundary logic. This completes the Crank–Nicolson implementation in computational space.

3.3.5 Memory and Runtime Considerations

A key motivation for adopting the Crank–Nicolson (CN) scheme lies in its favorable memory and computational complexity characteristics, particularly in comparison to spectral methods based on the Fast Fourier Transform (FFT).

Each Crank–Nicolson propagation step consists of solving a linear system involving tridiagonal matrices A and B , derived from the finite-difference discretization of the paraxial wave equation. These matrices are sparse, symmetric (modulo the complex diffusion coefficient), and constant throughout propagation. Once matrix A is LU-decomposed (e.g., via the Thomas algorithm), each propagation step reduces to two efficient operations: one matrix-vector product $B\mathbf{U}^n$, and one tridiagonal back-substitution to solve $A\mathbf{U}^{n+1} = B\mathbf{U}^n$.

The total runtime therefore scales linearly with the number of propagation steps:

$$\text{total runtime}_{\text{CN}} = N_z \times \mathcal{O}(J),$$

where J is the number of transverse grid points. Memory usage is equally modest: only a small number of vectors of length J are needed to store the solution and intermediate computations without loss of resolution. This makes the CN method not only more flexible in dealing with boundary conditions (such as radial Neumann BCs), but also competitive in runtime.

4 Results and Discussion

4.1 Preliminary tests in FFT

We begin by presenting key results from our split-step FFT simulations. First, we propagated a Gaussian beam (waist $w_0 = 4$ m, $\lambda = 400$ nm) over the full Earth–Moon distance $z = 3.844 \times 10^5$ km and investigated the evolutions of the intensity and waist over the distance z compared to the theoretical predictions.

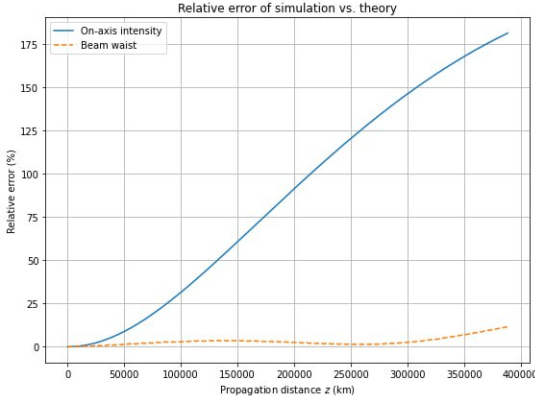


Figure 2: Relative error for waist and intensity evolutions using FFT.

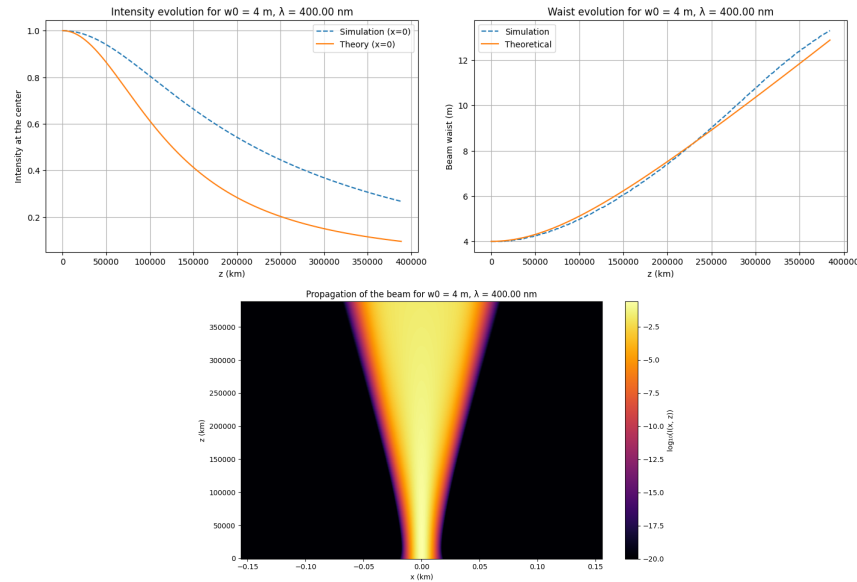


Figure 1: Waist and intensity evolutions compared to theoretical predictions with split-step FFT.

At first glimpse, both numerical and theoretical curves follow the same overall trend, but the simulated peak intensity at the Moon reaches 0.2667 (normalized) versus the theoretical 0.0948—giving a remarkable error of 181.3 %. In contrast, the beam-waist evolution is much closer to theory: the numerical waist remains within a few percent of the analytic $w(z)$ until about 3×10^5 km, beyond which sampling errors become noticeable.

Next, we tested a smaller waist ($w_0 = 0.1$ m) over a shorter path ($z = 300$ km). Again, the waist evolution remains in good agreement with theory, while the intensity deviates substantially.

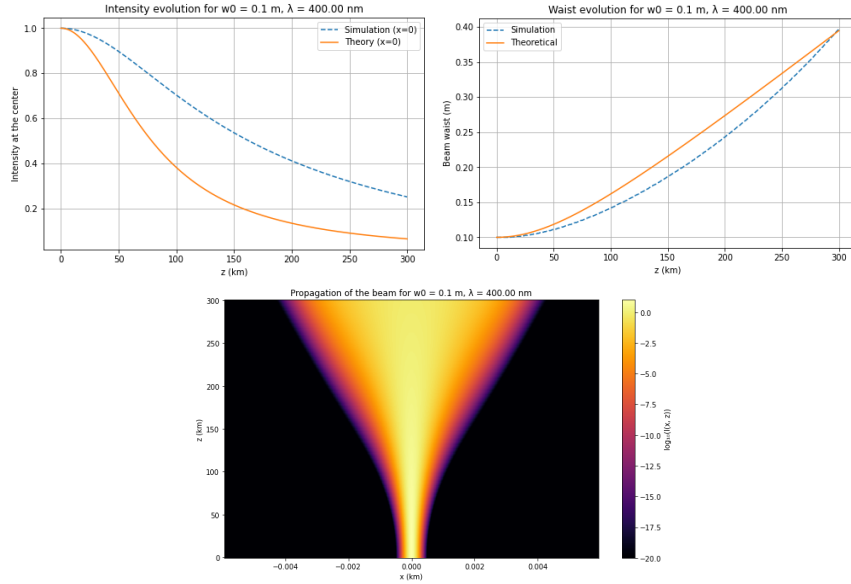


Figure 3: Waist and intensity evolutions compared to theoretical predictions with split-step FFT.

We notice that both simulations capture the expected physical behavior: a smaller waist diverges more rapidly (i.e., have a shorter Rayleigh range) —which is consistent with the $z_R \propto w_0^2$ scaling. Moreover, we found that reducing w_0 also requires proportionally reducing the propagation distance to maintain accurate numerical waists; specifically, the total distance z should remain within a few z_R , otherwise small normalization or sampling errors accumulate and distort the results.

We concluded that the split-step FFT method contain errors of implementation especially regarding the normalization that we operate at different stages of the propagation loops resulting in inaccuracies. We will therefore base the remaining of the analysis off the CN resolution scheme.

4.2 Implementing the Crank-Nicolson method

Initially, we modeled the propagation of our laser beam using the Crank–Nicolson (CN) numerical method directly in physical space. Although intuitive and straightforward to implement, this purely physical-space approach revealed substantial numerical issues as the propagation distance increased. We give below numerical data illustrating the performance of this technique.

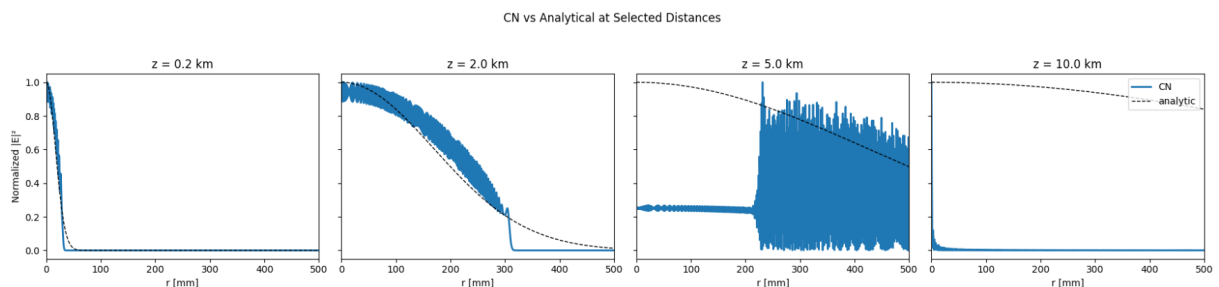


Figure 4: Model generation visualized over increasing distances

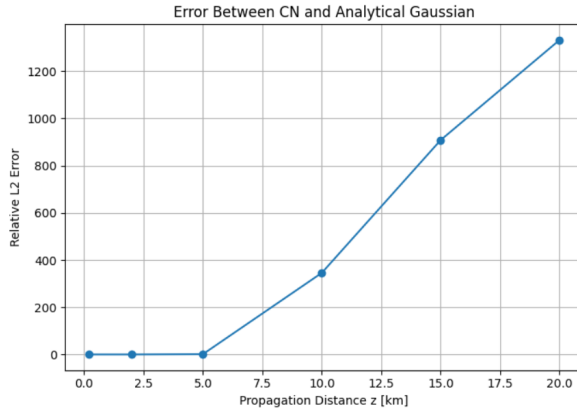


Figure 5: Evolution of error of CN method in a physical space model

We see from Figures 4 that at relatively short distances (e.g., $z = 0.2$, km), the numerical solution closely matches the analytical Gaussian beam solution, exhibiting minimal deviation. However, at ranges as short as $z = 2.0$, km and $z = 5.0$, km notable discrepancies become apparent, characterized by oscillations and increasingly large fluctuations in the field intensity profiles. Further, at $z = 10.0$, km and beyond, the intensity profiles become physically unrealistic. We quantify this degeneracy in Figure 5)and see the error increases quasi-linearly after a propagation distance of 5 km. These factors make the use of this technique inconceivable for simulations all the way to the Moon, some 384 400 km away.

We now turn to the alternative previously described in section ??, the application of the CN method in a computational space using cylindrical coordinates and absorption at the edges to prevent unwanted reflection effects. We display below the intensity profile of a Gaussian modeled with this technique overlaid with the analytical solution.

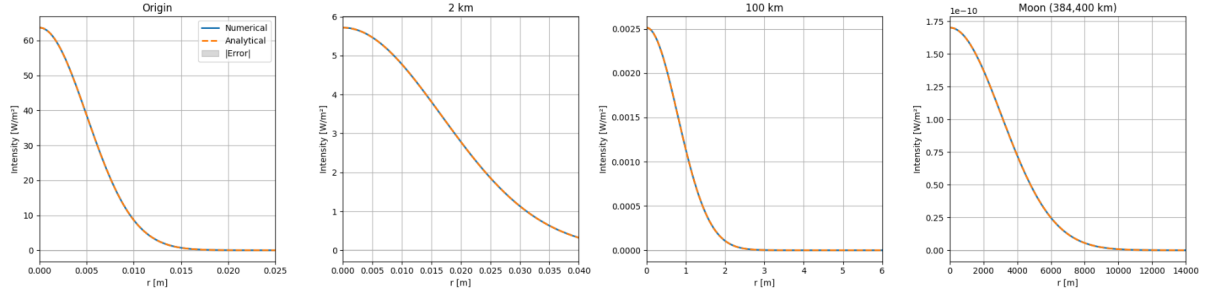


Figure 6: Computed and analytical intensity profiles for the propagation of a Gaussian at various distances

As illustrated in Figure 6, the simulated intensity profiles at the origin, 2 km, 100 km, and even at the lunar distance of 384 400 km remain in near-perfect agreement with the analytical prediction. The error is visually negligible across all scales, and no numerical artifacts or instabilities are present.

This confirms the Crank-Nicolson method in computational space as a robust and reliable approach for modeling diffraction-dominated beam propagation through vacuum for our application case.

To further characterize the propagation effects on the Gaussian beam, we present a series of numerical experiments.

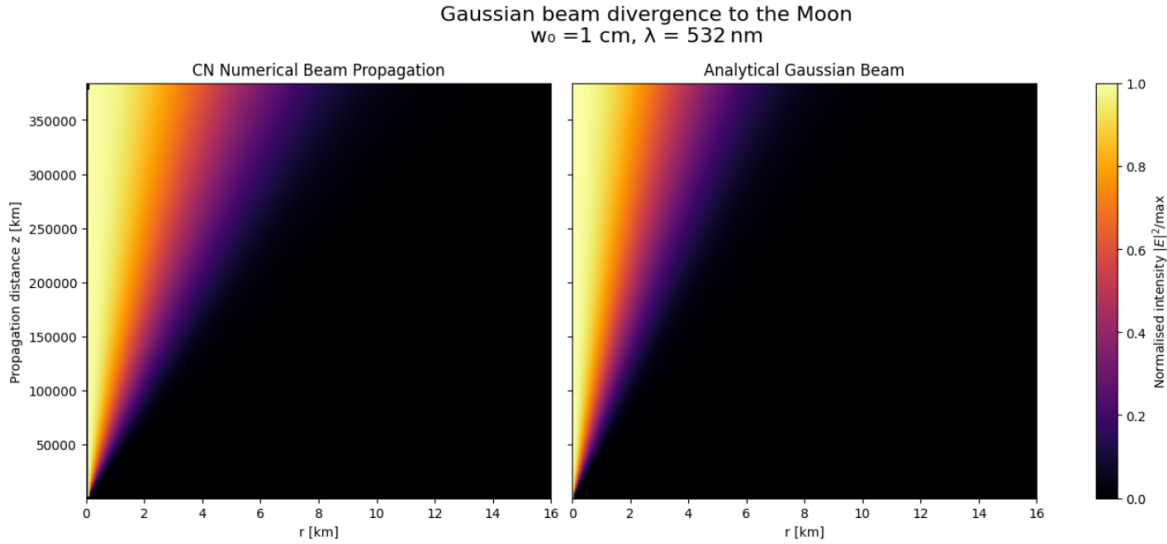


Figure 7: Visual comparison of analytically and numerically (using CN in computational space) propagated Gaussian beams

This further confirms that the expected analytical results and the results obtained from the CN method with computational space match.

4.3 Main observations

4.3.1 Initial parameter impacts

We first studied the effect of wavelength λ on the propagation behavior and uncovered a seemingly linear relationship suggesting that the spot size on the Moon scales with the wavelength at a fixed ratio of proportionality. This supports the fact that lower energy beams (at higher wavelengths) diffuse more over the same distance.

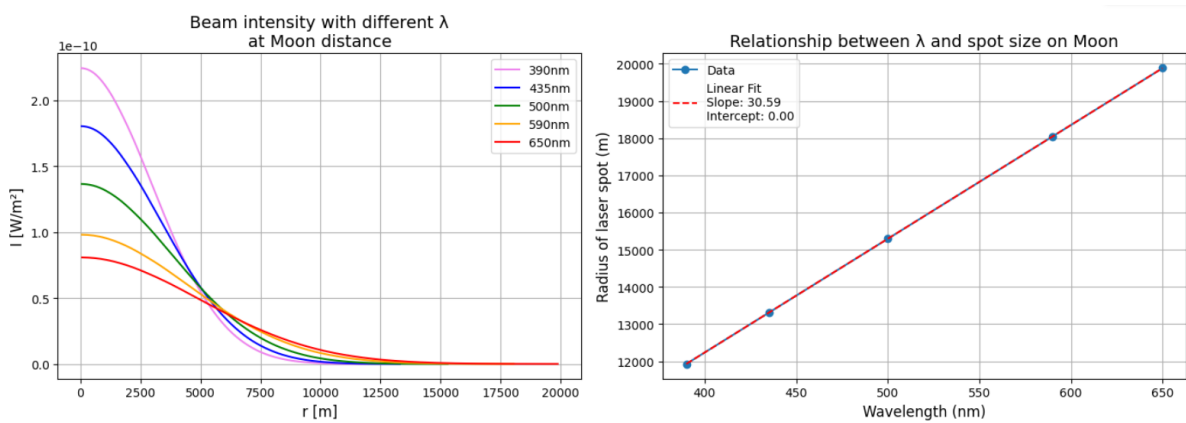


Figure 8: Effects of wavelength on intensity profile and final spot size on the Moon

Finally, we focus on the beam as it reaches the Moon and model the effects of changing the beam waist and power on the final intensity profile.

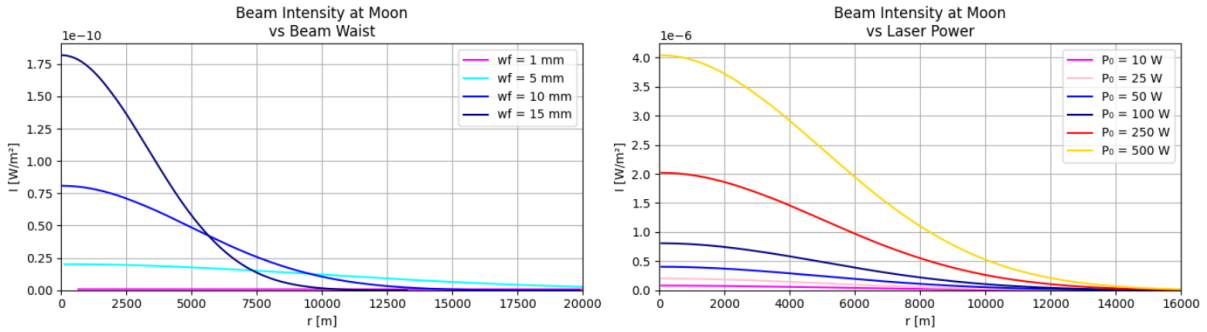


Figure 9: Left: effect of beam width on intensity profile at Moon. Right: effect of beam power on intensity profile at Moon

We see on the left of Figure 9 that increasing the beam waist through lower values greatly increases intensity at the Moon in a relationship stronger than proportionality. This indicates less diffraction, allowing the beam to maintain a tighter focus across the Earth–Moon distance. Thus, increasing the beam waist improves delivery efficiency over long distances, though it may be technically more difficult to achieve as it demands more careful optical alignment.

Additionally, we see on the right plot that peak intensity increases nearly linearly with laser power, while the beam shape remains nearly unchanged. We also confirm that the spatial extent of the beam is determined by diffraction and is unaffected by power. It is interesting to note that laser power is an effective parameter to scale intensity without modifying beam geometry.

4.3.2 Minimum Power Requirements for Lunar Applications

To estimate the minimum laser power P_0 required to detect a signal on the Moon, we consider a Gaussian beam whose on-axis intensity at distance z is given by:

$$I(0, z) = \frac{2P_0}{\pi w^2(z)}$$

where the beam radius $w(z)$ evolves with distance as:

$$w(z) = w_0 \sqrt{1 + \left(\frac{z}{z_R}\right)^2}, \quad \text{with } z_R = \frac{\pi w_0^2}{\lambda}$$

We seek a minimum power P_0 such that $I(0, z = D) \geq I_{\text{target}}$, which yields:

$$P_0 \geq \frac{\pi}{2} w_0^2 \left[1 + \left(\frac{D\lambda}{\pi w_0^2} \right)^2 \right] I_{\text{target}}$$

This formula allows us to estimate the minimum required initial power for achieving a target intensity on the Moon given a beam waist w_0 , wavelength λ , and propagation distance D . To illustrate practical relevance, we compute this required power for three different mission scenarios using $w_0 = 10 \text{ mm}$ and $\lambda = 500 \text{ nm}$:

- **Lunar Laser Ranging (LLR):** Detecting a faint return signal from lunar retroreflectors requires only $I_{\text{target}} = 1 \mu\text{W}/\text{m}^2$. The required initial power is about 59 W.
- **Lunar Communication:** For transmitting data to the Moon via laser, a target intensity of $1 \text{ mW}/\text{m}^2$ implies a required power of 59 kW.
- **Surface Heating:** Delivering thermal energy for surface interaction requires $1 \text{ kW}/\text{m}^2$, which translates to a massive 59 MW of laser power.

To visualize the power delivery efficiency, we simulated the beam footprint on the Moon for each scenario. The following plots show how peak power density scales while the spatial extent of the beam remains constant:

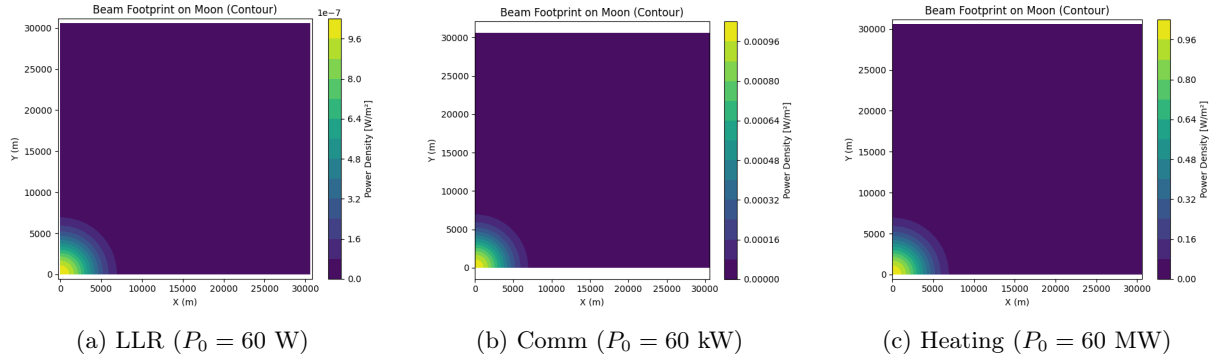


Figure 10: Beam footprints on the Moon for increasing laser powers. The spot size is diffraction-limited and identical in all cases; only peak intensity scales.

From these calculations and visualizations, it is evident that only the LLR-level application is comfortably achievable with today's laser technology. A 60 W system is well within the reach of commercial or research-grade pulsed lasers. For the communication case, the 60 kW requirement begins to stretch the bounds of practicality, especially for continuous-wave operation. Nevertheless, pulsed or space-based lasers could make it viable. The surface heating scenario remains out of reach due to energy, thermal, and optical challenges.

Table 1: Summary of minimum required laser powers for various lunar mission types.

Mission Type	Target Intensity	Required Power P_0	Feasibility	Notes
Lunar Laser Ranging	1 $\mu\text{W}/\text{m}^2$	~ 60 W	Yes	Easily achievable with current systems.
Lunar Communication	1 mW/m^2	~ 60 kW	Partially	Challenging but possible with specialized systems.
Surface Heating	1 kW/m^2	~ 60 MW	Not currently	Orders of magnitude beyond current Earth-based or mobile laser capacity.

A more detailed table of simulation results including wavelength, beam waist, and power data is provided in Appendix D.

4.3.3 Square Beam Envelope

A non-Gaussian profile we explored is the square beam envelope, which is characterized by a flat, constant amplitude within a defined width and zero outside. This sharp-edged profile is useful for testing the diffraction response of beams with abrupt intensity transitions. It also approximates a simplified top-hat laser beam, which could be relevant for engineered beam shaping in practical laser systems.

Figure 11 shows the initial envelope used in our simulation. The beam is sharply defined over a finite range in ξ , with high intensity in the center and sharp cutoffs at the edges.

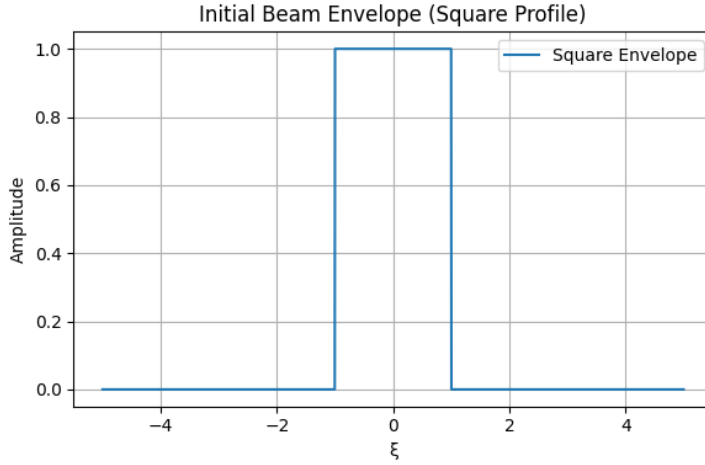


Figure 11: Initial beam envelope used in the square beam simulation. Constant amplitude within a defined region, zero elsewhere.

To observe the square beam's propagation characteristics, Figure 12 presents a 2D intensity map from Earth to Moon. The sharply bounded beam exhibits significant diffraction effects, with sidelobes forming early and persisting across long distances. The beam's central core spreads out more than Gaussian-based profiles, and interference features remain prominent due to the abrupt edges in the initial envelope.

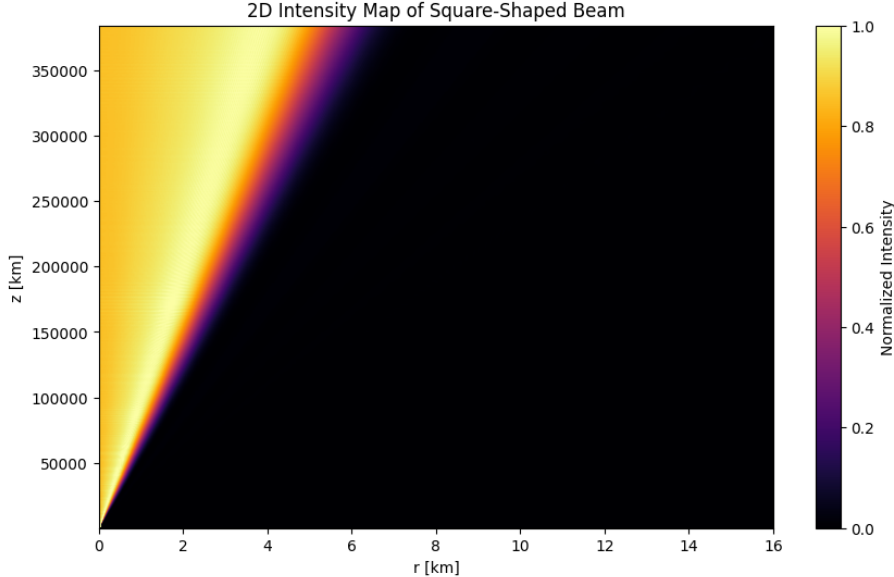


Figure 12: 2D intensity map of square beam propagation over Earth–Moon distance. Strong diffraction and interference patterns emerge from sharp beam edges.

Figure 13 further illustrates this behavior through radial intensity profiles at increasing propagation distances. We observe that at short range (1 km), the square beam maintains its shape but already shows early sidelobe formation. Then at longer distances, especially 100 km and beyond, sidelobes intensify and dominate the outer profile. Finally at the Moon's distance, the beam has spread substantially, with only a faint central maximum remaining and visible ring structures.

These findings suggest that while square beams provide useful insight into diffraction-limited propagation, their hard edges introduce strong instability and interference that limit their practical use for long-range focused beam delivery.

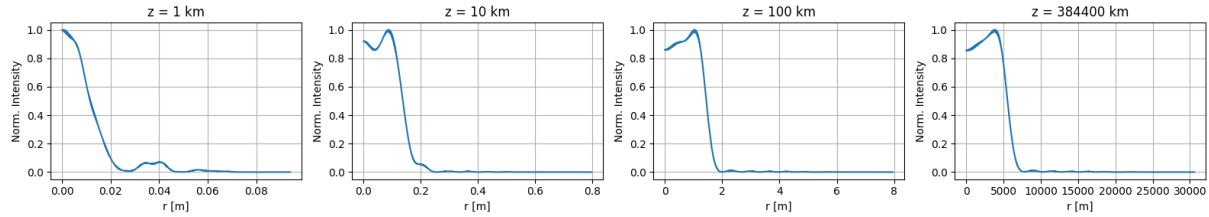


Figure 13: Normalized intensity profiles of a square beam at various propagation distances. Edge-induced diffraction causes rapid beam broadening and ring-like interference.

4.3.4 Super-Gaussian Envelope

In addition to standard Gaussian profiles, we also investigated the behavior of Super-Gaussian beam envelopes, which are characterized by the form $\exp(-r^{2n})$ with order $n \geq 1$. Super-Gaussians are attractive for long-distance propagation because their flatter central profile and sharper edges offer the potential for a more confined beam with reduced sidelobe intensity.

Figure 14 presents a 2D intensity map of a Super-Gaussian beam of order $n = 4$, showing the radial intensity distribution as a function of propagation distance z . The beam maintains a narrow, high-intensity core with sharply defined edges, suggesting strong confinement across the entire trajectory to the Moon.

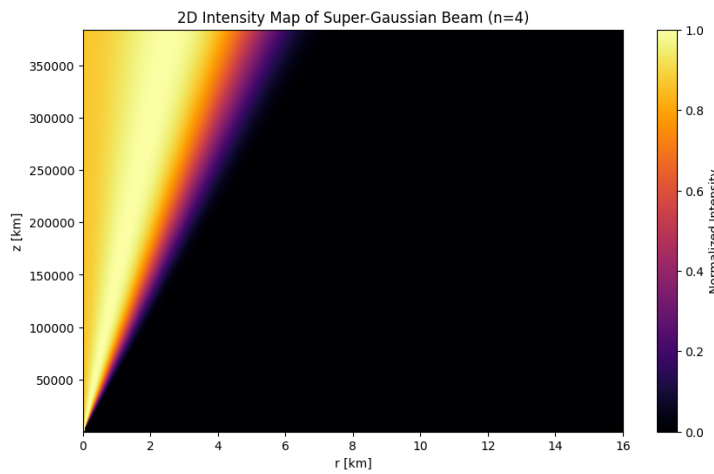


Figure 14: 2D Intensity map of a Super-Gaussian beam (order $n = 4$) as it propagates from Earth to Moon. Intensity remains strongly confined along the beam axis with sharp lateral boundaries.

To illustrate this confinement behavior at specific points along the propagation path, Figure 15 shows normalized radial intensity profiles at increasing distances (1 km, 10 km, 100 km, and 384,400 km). The profile retains a steep falloff and narrow spot size, even after hundreds of thousands of kilometers, demonstrating the practical utility of higher-order beam shaping.

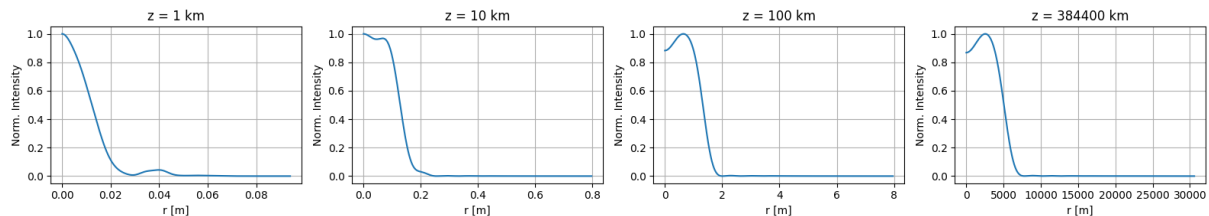


Figure 15: Snapshots of normalized intensity profiles of a Super-Gaussian ($n = 4$) beam at selected propagation distances. Beam maintains tight confinement and sharp decay edges over extremely long distances.

Finally, to quantify the impact of the Super-Gaussian order on beam divergence, we measured the spot radius on the Moon for different orders. The order n controls the beam shape: low orders resemble standard Gaussians with smooth roll-off, while higher orders produce flatter, more uniform intensity across the beam core with sharper edges. As shown in Figure `effig:sg-divergence`, increasing the order significantly affects the beam's far-field behavior. Although higher orders offer improved confinement over short to medium distances, beyond a certain point they can exacerbate diffraction at very long ranges. This leads to a sharp increase in spot size on the Moon. Therefore, our results suggest that there is an optimal Super-Gaussian order that balances near-field beam shaping with long-range propagation efficiency.

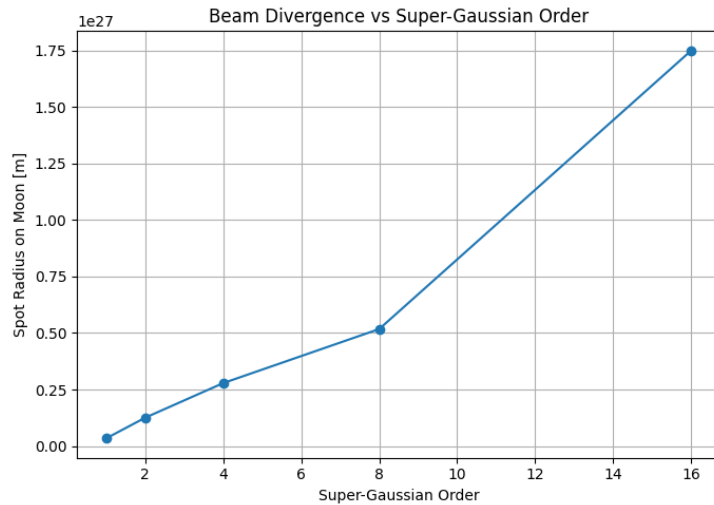


Figure 16: Spot radius on the Moon as a function of Super-Gaussian order. Beyond a certain order, divergence grows rapidly, indicating a trade-off in beam shaping.

4.3.5 Noisy-Gaussian Envelope

To simulate the irregularities introduced by atmospheric turbulence or imperfections in real laser systems, we experimented with a noisy Gaussian envelope. This profile is based on a standard Gaussian function with superimposed low- and high-frequency perturbations, intended to mimic the kinds of distortions a beam might encounter in practice.

Figure 17 shows the initial amplitude of the noisy Gaussian. The perturbations create localized peaks and valleys, which offer a way to examine how beam integrity degrades or stabilizes over long-distance propagation.

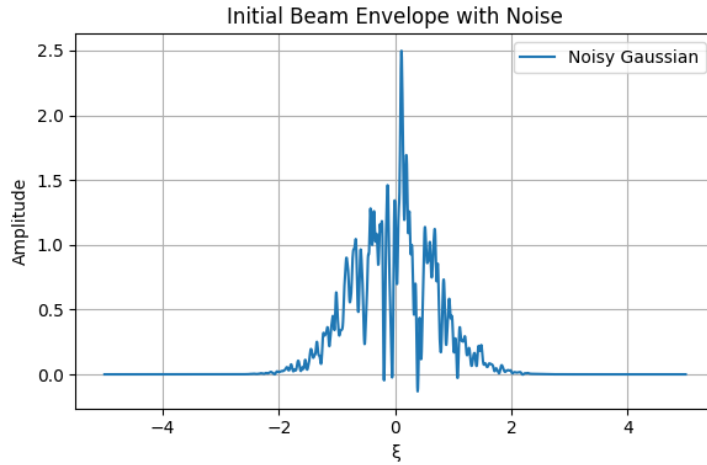


Figure 17: Initial beam envelope: a Gaussian profile with added synthetic noise to mimic atmospheric distortions.

Figure 18 illustrates the beam's full propagation as a 2D intensity map. Despite the noise-induced irregularities in the initial profile, the beam maintains a relatively clean and symmetric structure over long distances. The central peak dominates the profile, and the noisy features largely dissipate due to natural diffraction.

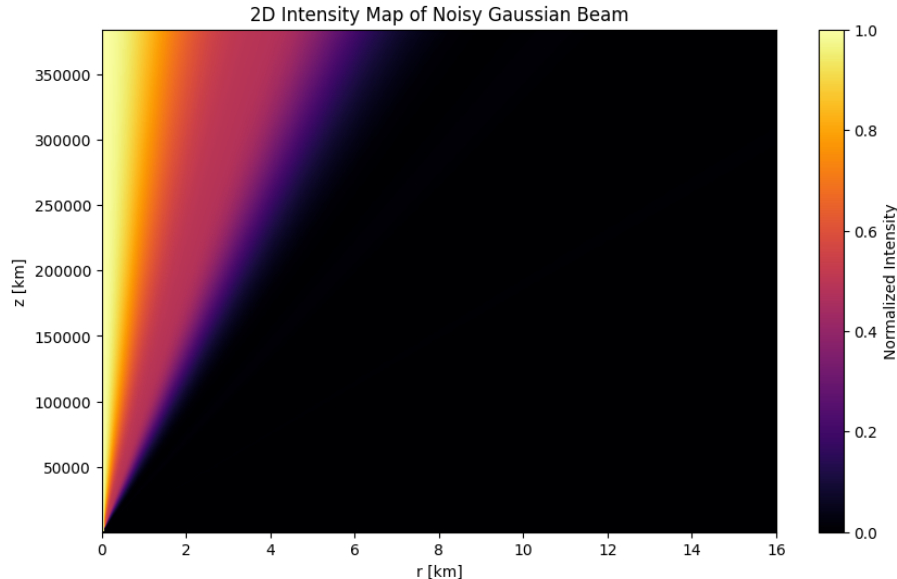


Figure 18: 2D intensity map of a noisy Gaussian beam propagating to the Moon. Central peak remains dominant, with minimal visible effects from initial noise.

To examine the stability of the beam further, Figure 19 presents normalized intensity profiles at increasing distances. Notably, at short distances, small-scale fluctuations from noise are still apparent. As the beam propagates, these fluctuations smooth out, and the profile resembles that of a clean Gaussian. Finally at lunar distances, the noise-induced features have almost completely disappeared, confirming strong self-regularization through diffraction.

These results are encouraging for the feasibility of real-world laser transmission, showing that moderate envelope noise may not significantly affect beam delivery over long distances.

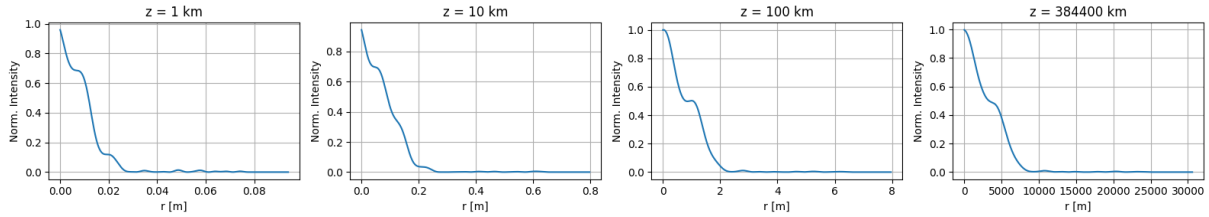


Figure 19: Radial intensity profiles of the noisy Gaussian beam at increasing distances. The beam self-stabilizes, and initial irregularities vanish due to diffraction.

4.4 General Discussion : Answering the Central Question.

The core objective of this project was to investigate: *How does the laser beam from a laser pointer travel to the Moon?* Through a series of progressively refined simulations, we analyzed various beam envelopes and propagation techniques to determine which configurations are most effective for transmitting light across the vast 384,400 km separating Earth and Moon.

Beam Parameter Sensitivity. We previously explored how physical parameters affect beam evolution and observed that the beam spot size on the Moon increases linearly with wavelength, confirming that longer-wavelength beams diffract more readily (Figure 8). Lower wavelengths are thus preferable when seeking higher intensity and tighter focus.

We also demonstrated that increasing beam waist significantly enhances the beam's confinement over distance (Figure 9, left). A wider waist leads to reduced diffraction, which makes it more suitable for long-range propagation, although it may be harder to produce and align optically.

Meanwhile, to determine whether such beams could deliver detectable signals or usable power to the Moon, we analytically derived and numerically verified the minimum power P_0 required to achieve a target intensity at the lunar surface. Depending on the application—ranging from passive detection to communication or energy transmission—intensity targets vary by many orders of magnitude.

Exploring Non-Gaussian Envelopes. The results further examined how initial envelope shape affects long-distance delivery. Square beams suffered from pronounced diffraction and edge-driven interference patterns (Figure 12 and 13). These findings demonstrated that abrupt transitions in amplitude are detrimental for lunar-scale applications.

In contrast, Super-Gaussian envelopes (Figure 14) maintained strong axial confinement across distances. They preserved a narrow spot even at the Moon, with fewer oscillations compared to square beams. However, higher-order Super-Gaussians showed diminishing returns: while initially beneficial, orders beyond $n = 8$ caused rapid growth in spot size due to diffraction effects (Figure 16). This underscores a key trade-off—flatter central profiles improve short-range confinement but can become detrimental at long range.

Finally, the noisy Gaussian (Figure 17) provided a practical testbed for real-world imperfections such as turbulence or laser instability. Despite significant initial perturbations, the beam self-regularized during propagation (Figure 18 and 19). This result supports the hypothesis that moderate imperfections will not critically impair transmission to the Moon, provided the envelope is fundamentally smooth and centered.

Feasibility and Limitations. Overall, the results affirm the feasibility of modeling and predicting laser beam propagation to the Moon. Using computational Crank–Nicolson methods with cylindrical symmetry and realistic envelopes, we observed strong agreement with theoretical predictions, sensitivity to physical parameters, and resilience to moderate noise. However, the model makes many idealizing assumptions: no scattering, no absorption, no turbulence, and perfect alignment. These significantly inflate our projected performance—under such ideal conditions, source-to-target efficiency can reach up to 10–15%. In contrast, real-world scenarios involving atmospheric losses, alignment drift, and optical imperfections could reduce this efficiency to below 0.01%, making high-power delivery particularly challenging.

4.4.1 Constructing the Perfect Laser

Based on all prior results, we now synthesize what might constitute the *perfect* laser beam for reaching the Moon. Such a beam would aim to maximize power density at the lunar surface while minimizing beam spread and instabilities :

- The **envelope** should be near-Gaussian or moderately Super-Gaussian (e.g., order $n = 4$ to $n = 6$), avoiding sharp edges that induce diffraction rings but also avoiding very flat-top shapes that diverge quickly.
- The **wavelength** should be as short as feasible, ideally in the visible to near-UV range ($\lambda \approx 400\text{--}500$ nm), to reduce diffraction. However, absorption and atmospheric transmission (if used terrestrially) must also be considered.
- The **beam waist** should be large—on the order of several centimeters—to reduce divergence. In our simulations, waist values of 10–15 mm significantly improved spot confinement.
- The **initial power** must be high to yield detectable intensities at the Moon. If the final spot radius on the Moon is approximately 2 km (from the best Gaussian case), the spot area is $A = \pi R^2 = \pi(2000)^2 \approx 1.26 \times 10^7$ m². If our simulation yields a central intensity of $I = 10^{-10}$ W/m², then the received power is $P = I \cdot A \approx 1.26\text{mW}$. Working backwards, if this results from a 10 mW beam, the system efficiency is roughly 12.6%. In reality, due to absorption, scattering, and atmospheric distortion, this number would be much lower—possibly less than 0.01% for Earth-based sources.

Thus, answering our main question: *A laser beam from a pointer can indeed travel to the Moon, and its behavior over this journey can be accurately modeled with computational beam propagation techniques. However, delivering usable power or detectable signals at such distances remains heavily constrained by beam divergence, diffraction, and real-world losses.*

5 Conclusions

This project set out to determine how a laser beam propagates from Earth to the Moon and what physical and numerical constraints govern this process. By modeling beam evolution under the paraxial approximation and implementing robust numerical methods—particularly the Crank–Nicolson scheme in computational space—it was shown that accurate simulation of long-distance propagation is both feasible and essential to understanding beam divergence and energy loss.

The results confirm that the final intensity and footprint of a laser beam at lunar distances are primarily governed by diffraction, with strong dependence on the initial beam waist, wavelength, and envelope shape. Broader beams and shorter wavelengths reduce divergence, and super-Gaussian profiles offered improved confinement over standard Gaussians. Simulations with noise showed that initial irregularities dissipate during propagation, indicating robustness under idealized conditions.

The study emphasized the need to align theoretical assumptions with stable numerical schemes. Approximations such as the paraxial and slowly-varying envelope assumptions proved effective but require careful treatment, particularly with proper normalization and scaling. Transformation into computational space was a key step, enabling simulations over astronomical distances without artificial boundary effects.

The simulations, however, had notable limitations. They assumed vacuum propagation and neglected absorption, scattering, turbulence, nonlinearities, and optical imperfections. Beam alignment was treated as ideal. Thus, the estimated efficiencies and required power levels are optimistic; practical implementations would face significantly higher losses.

The findings show that using dynamic coordinate systems early in the modeling process is crucial for large-scale propagation. Verifying numerical accuracy against analytical solutions was essential for stability, and boundary absorption and beam shaping techniques proved effective for managing complex profiles.

In summary, this project establishes a reliable framework for simulating laser beam propagation over astronomical distances, clarifying the key physical effects, numerical strategies, and practical constraints involved in such systems.

6 Appendix

A Code Repository

All code implementations developed for this project, including simulation scripts and visualization tools, are available at the following link:

Project code repository

B Derivation of the Paraxial Wave Equation

We consider a scalar electric field $E(\vec{r}, t)$ expressed as the product of a slowly varying envelope $\mathcal{E}(\vec{r}, t)$ and a rapidly oscillating carrier wave:

$$E(\vec{r}, t) = \mathcal{E}(\vec{r}, t)e^{i(k_0 z - \omega_0 t)} \quad (1)$$

where k_0 and ω_0 are the central wavevector and angular frequency, respectively.
Starting from the scalar wave equation: d'Alembert equation:

$$\nabla^2 E - \frac{1}{c^2} \frac{\partial^2 E}{\partial t^2} = 0 \quad (2)$$

we expand the spatial and temporal derivatives. The Laplacian becomes:

$$\nabla^2 E = e^{i(k_0 z - \omega_0 t)} \left(\nabla_{\perp}^2 \mathcal{E} + \frac{\partial^2 \mathcal{E}}{\partial z^2} + 2ik_0 \frac{\partial \mathcal{E}}{\partial z} - k_0^2 \mathcal{E} \right) \quad (3)$$

where ∇_{\perp}^2 denotes the transverse Laplacian $\frac{\partial^2}{\partial x^2} + \frac{\partial^2}{\partial y^2}$.

Now let us introduce the moving frame coordinates:

$$\xi = z \quad (\text{propagation distance}) \quad (4)$$

$$\tau = t - \frac{z}{c} \quad (\text{retarded time}) \quad (5)$$

First Derivatives

Using the chain rule:

$$\frac{\partial \mathcal{E}}{\partial z} = \frac{\partial \mathcal{E}}{\partial \xi} \frac{\partial \xi}{\partial z} + \frac{\partial \mathcal{E}}{\partial \tau} \frac{\partial \tau}{\partial z} = \frac{\partial \mathcal{E}}{\partial \xi} - \frac{1}{c} \frac{\partial \mathcal{E}}{\partial \tau} \quad (6)$$

$$\frac{\partial \mathcal{E}}{\partial t} = \frac{\partial \mathcal{E}}{\partial \tau} \frac{\partial \tau}{\partial t} = \frac{\partial \mathcal{E}}{\partial \tau} \quad (7)$$

Second Derivatives

$$\frac{\partial^2 \mathcal{E}}{\partial z^2} = \frac{\partial^2 \mathcal{E}}{\partial \xi^2} - \frac{2}{c} \frac{\partial^2 \mathcal{E}}{\partial \xi \partial \tau} + \frac{1}{c^2} \frac{\partial^2 \mathcal{E}}{\partial \tau^2} \quad (8)$$

$$\frac{\partial^2 \mathcal{E}}{\partial t^2} = \frac{\partial^2 \mathcal{E}}{\partial \tau^2} \quad (9)$$

(10)

Substituting into the scalar wave equation:

$$\nabla_{\perp}^2 \mathcal{E} + \left(\frac{\partial^2 \mathcal{E}}{\partial \xi^2} - \frac{2}{c} \frac{\partial^2 \mathcal{E}}{\partial \xi \partial \tau} + \frac{1}{c^2} \frac{\partial^2 \mathcal{E}}{\partial \tau^2} \right) + 2ik_0 \left(\frac{\partial \mathcal{E}}{\partial \xi} - \frac{1}{c} \frac{\partial \mathcal{E}}{\partial \tau} \right) - \frac{1}{c^2} \frac{\partial^2 \mathcal{E}}{\partial \tau^2} = 0 \quad (11)$$

After simplifying the terms that cancel out and applying the slow envelope approximation. Indeed, the envelope \mathcal{E} varies over much larger distances than the optical wavelength

$$\left| \frac{\partial^2 \mathcal{E}}{\partial \xi^2} \right| \ll \left| 2k_0 \frac{\partial \mathcal{E}}{\partial \xi} \right| \quad (12)$$

$$(13)$$

The envelope \mathcal{E} varies much slower in time than the carrier wave:

$$\left| \frac{\partial^2 \mathcal{E}}{\partial \xi \partial \tau} \right| \ll \left| \frac{k_0}{c} \frac{\partial \mathcal{E}}{\partial \tau} \right| \quad (14)$$

We obtain :

$$\nabla_{\perp}^2 \mathcal{E} + 2ik_0 \left(\frac{\partial \mathcal{E}}{\partial \xi} + \frac{1}{c} \frac{\partial \mathcal{E}}{\partial \tau} \right) = 0 \quad (15)$$

B.1 Stationary Envelope Approximation

If the envelope is stationary, meaning that \mathcal{E} depends only on (x, y, z) and not on time t , $(\partial \mathcal{E} / \partial \tau = 0)$ the equation simplifies further to the standard paraxial wave equation.

$$\boxed{\nabla_{\perp}^2 \mathcal{E} + 2ik_0 \frac{\partial \mathcal{E}}{\partial z} = 0} \quad (16)$$

This equation describes the evolution of the complex amplitude $\mathcal{E}(x, y, z)$ of a laser beam propagating predominantly along the z -axis, under the assumptions of small diffraction angles and slow variations.

C Complexity Analysis of FFT vs. DFT

C.1 Naive DFT Complexity

Given a signal f_n of length N , the Discrete Fourier Transform is:

$$\hat{f}_k = \sum_{n=0}^{N-1} f_n e^{-2\pi i k n / N}, \quad k = 0, 1, \dots, N-1.$$

This requires N operations for each of the N output points, yielding:

$$\text{Total complexity: } \mathcal{O}(N^2).$$

C.2 Fast Fourier Transform (FFT) Complexity

The Fast Fourier Transform (FFT) uses a divide-and-conquer strategy by recursively breaking the DFT of size N into two DFTs of size $N/2$, one for even-indexed elements and one for odd-indexed elements. Using FFT, this can be rewritten as:

$$\hat{f}_k = \sum_{n=0}^{N/2-1} f_{2n} e^{-2\pi i k (2n) / N} + \sum_{n=0}^{N/2-1} f_{2n+1} e^{-2\pi i k (2n+1) / N}$$

Each recursion level performs $\mathcal{O}(N)$ operations to combine the results of the smaller FFTs. Since the size is halved at each step, there are $\log_2 N$ recursion levels. Hence, the total complexity is:

$$\mathcal{O}(N \log N)$$

This is a significant improvement over the naive DFT algorithm, which has a complexity of $\mathcal{O}(N^2)$.

D Data for parameter variations

Table 2: Detailed power requirements and resulting spot characteristics for different mission types and beam configurations.

λ (nm)	w_0 (mm)	I_{target} (W/m ²)	P_0 (W)	Peak I (W/m ²)	Spot Radius (m)
<i>Lunar Laser Ranging (LLR)</i>					
400	5	1×10^{-6}	1.5×10^2	1.00×10^{-6}	48943.33
400	5	1×10^{-6}	3.0×10^2	2.00×10^{-6}	48943.33
400	10	1×10^{-6}	3.8×10^1	1.00×10^{-6}	24471.66
400	10	1×10^{-6}	7.5×10^1	2.00×10^{-6}	24471.66
500	5	1×10^{-6}	2.4×10^2	1.00×10^{-6}	61179.16
500	5	1×10^{-6}	4.7×10^2	2.00×10^{-6}	61179.16
500	10	1×10^{-6}	5.9×10^1	1.00×10^{-6}	30589.58
500	10	1×10^{-6}	1.2×10^2	2.00×10^{-6}	30589.58
600	5	1×10^{-6}	3.4×10^2	1.00×10^{-6}	73414.99
600	5	1×10^{-6}	6.8×10^2	2.00×10^{-6}	73414.99
600	10	1×10^{-6}	8.5×10^1	1.00×10^{-6}	36707.50
600	10	1×10^{-6}	1.7×10^2	2.00×10^{-6}	36707.50
<i>Lunar Communication</i>					
400	5	1×10^{-3}	1.5×10^5	1.00×10^{-3}	48943.33
400	5	1×10^{-3}	3.0×10^5	2.00×10^{-3}	48943.33
400	10	1×10^{-3}	3.8×10^4	1.00×10^{-3}	24471.66
400	10	1×10^{-3}	7.5×10^4	2.00×10^{-3}	24471.66
500	5	1×10^{-3}	2.4×10^5	1.00×10^{-3}	61179.16
500	5	1×10^{-3}	4.7×10^5	2.00×10^{-3}	61179.16
500	10	1×10^{-3}	5.9×10^4	1.00×10^{-3}	30589.58
500	10	1×10^{-3}	1.2×10^5	2.00×10^{-3}	30589.58
600	5	1×10^{-3}	3.4×10^5	1.00×10^{-3}	73414.99
600	5	1×10^{-3}	6.8×10^5	2.00×10^{-3}	73414.99
600	10	1×10^{-3}	8.5×10^4	1.00×10^{-3}	36707.50
600	10	1×10^{-3}	1.7×10^5	2.00×10^{-3}	36707.50
<i>Surface Heating</i>					
400	5	1×10^3	1.5×10^{11}	1.00×10^3	48943.33
400	5	1×10^3	3.0×10^{11}	2.00×10^3	48943.33
400	10	1×10^3	3.8×10^{10}	1.00×10^3	24471.66
400	10	1×10^3	7.5×10^{10}	2.00×10^3	24471.66
500	5	1×10^3	2.4×10^{11}	1.00×10^3	61179.16
500	5	1×10^3	4.7×10^{11}	2.00×10^3	61179.16
500	10	1×10^3	5.9×10^{10}	1.00×10^3	30589.58
500	10	1×10^3	1.2×10^{11}	2.00×10^3	30589.58
600	5	1×10^3	3.4×10^{11}	1.00×10^3	73414.99
600	5	1×10^3	6.8×10^{11}	2.00×10^3	73414.99
600	10	1×10^3	8.5×10^{10}	1.00×10^3	36707.50
600	10	1×10^3	1.7×10^{11}	2.00×10^3	36707.50

To complement the study of the impact of the variation of initial parameter above, we compiled a comprehensive dataset of simulation results covering a wide range of wavelengths, beam waists, and application intensities. The following table presents the minimum required laser power P_0 , peak power

density, and resulting spot size on the Moon for each case. The entries are grouped by application type to highlight how performance requirements vary across scientific, communication, and energy delivery scenarios.

Contributions

We tried dividing each task of the project in the best way possible.

- Timothey organized the outline and structure of our project and determined which results we were looking for.
- The introduction was written by Elsa.
- Elsa, Yasmine and Victoria worked on the theoretical part. The derivation of the paraxial wave equation was done by Elsa and Victoria , while the paragraph on the Gaussian Beam solutions was written by Yasmine.
- The numerical implementation part was collectively written by Victoria (Discretization, Dynamic window and Split- step method), Elsa (entire FFT part), and Yasmine (Entire Crank Nicolson part)
- Victoria and Elsa worked on implementing the FFT method on the computer, while Yasmine and Timothey focused on implementing the Crank- Nicolson method.
- We collectively worked on analyzing the results. Elsa and Victoria worked on the FFT results, while Yasmine and Timothey analyzed the CN, and Yasmine finalized with the general results.
- The conclusion was written by Timothey and Yasmine.

References

1. Arnaud Couairon, *Numerical method for scaling box size with propagation distance* (2024).
2. A. Couairon, E. Brambilla, T. Corti, D. Majus, O. de J. Ramírez-Góngora, and M. Kolesik, *Practitioner's guide to laser pulse propagation models and simulation* (EDP Sciences, Berlin, 2011), pp. 39–41.
3. A. Couairon, *Lecture Notes for PHY571* (2024).